Using Neutron Reflectometry to Discern the Structure of Fibrinogen Adsorption at the Stainless Steel/Aqueous Interface

Mary H. Wood[1*], Kathryn L. Browning[1], Robert D. Barker[2], Stuart M. Clarke[1]

[1]*Department of Chemistry, University of Cambridge, Lensfield Road, Cambridge, CB2 1EW, UK*

[2]*Institut Laue-Langevin, 71 avenue des Martyrs, CS 20156, 38042 Grenoble cedex 9, France.*

Current address: School of Science & Engineering, University of Dundee, Dundee, DD1 4HN, UK

**mw531@cam.ac.uk, (+44)1223 765700*

Abstract

Neutron reflectometry has been successfully used to study adsorption on a stainless steel surface by means of depositing a thin steel film on silicon. The film was characterized using XPS (X-ray photoelectron spectroscopy), TOF-SIMS (time-of-flight secondary ion mass spectrometry) and GIXRD (grazing incidence X-ray diffraction), demonstrating the retention both of austenitic phase and of the required composition for 316L stainless steel. The adsorption of fibrinogen from a physiologically-relevant solution onto the steel surface was studied using neutron reflectometry and QCM (quartz crystal microbalance) and compared to that on a deposited chromium oxide surface. It was found that the protein forms an irreversibly-bound layer at low concentrations, with maximum protein concentration a distance of around 20 Å from the surface. Evidence for a further diffuse reversibly-bound layer forming at higher concentrations was also observed. Both the structure of the layer revealed by the neutron reflectometry data and the high water retention predicted by the QCM data suggest that there is a significant extent of protein unfolding upon adsorption. A lower extent of adsorption was seen on the chromium surfaces, although the adsorbed layer structures were similar, suggesting comparable adsorption mechanisms.

Introduction

The study of protein adsorption onto stainless steel surfaces has attracted considerable interest for many years, not least due to its well-established role as a key structural biomaterial, having been used to treat fractures since the 1890s[1]. 316L stainless steel is one of the most prevalent surgical grades and is used both for surgical instruments and as a standard material for implants including stents and screws, amongst many others. Whilst the superior biocompatibility and lower density of titanium makes it the preferred option for many long-term implants, the properties of stainless steel are still adequate for most structural applications, and its lower cost renders it the material of choice when using titanium is unecessary[2,3].

The stainless quality of austenitic 316L steel is universally attributed to the formation of a passive oxide/hydroxide surface film, generally quoted as having a thickness between 1 and 4 nm[4–9]. This film is known to be significantly enriched in chromium (reported to be around or above 50 % greater than the bulk concentration). There is an abundance of literature concerning the passive film formed on stainless steels, and it has been well-reviewed in 1984 by Fischmeister *et al*.[7] and further by Olsson *et al*. in 2003[8]. In brief, the current understanding is of a three-layer model, with the uppermost comprising the passive oxide film, enriched in chromium and molybdenum (but with the other alloying elements effectively absent), an interlayer of depth a few atomic layers immediately beneath that is enriched in nickel and manganese and finally the bulk alloy[10]. The level of chromium enrichment is believed to vary somewhat throughout the passive oxide film, with the peak concentration occurring a few angstroms down into the film; the actual surface is highly

enriched in oxygen with a slight metal depletion. The chromium level peaks and then gradually lessens with depth into the oxide film[11].

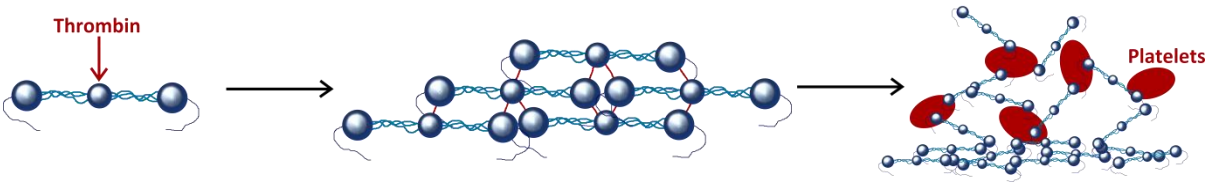

Figure 1. Simplified schematic depicting the involvement of fibrinogen within the complex coagulation cascade.

Proteins are known to adsorb to biomaterial surfaces within seconds of implantation, arriving there shortly after the immediate formation of a surface water layer whose structure will influence the manner of protein interaction thereupon[12]. Larger, more slowly moving cells, including inflammatory cells and the bacteria responsible for biomaterials-associated infection (BAI), arrive later and so confront a surface of proteins, rather than the biomaterial itself. The way in which proteins interact with the biomaterial surface is critical, therefore, in determining the success or rejection of the implant, and hence understanding and predicting their adsorption behavior is crucial[13–16].

An important aspect of protein adsorption in general is the tendency of the proteins to undergo conformational changes upon adsorption. For example, proteins that are folded such that the majority of their hydrophobic residues are hidden within their bulk structure when surrounded by water may relax upon adsorption onto a more hydrophobic surface and reorient to maximise the hydrophobic interactions. Additionally, proteins that initially adsorb via a small number of binding sites may subsequently unfold in order to increase their adsorption footprint, subject to an absence of neighbouring adsorbed species. Such changes may lead to multilayer adsorption even for proteins that do not exist as aggregates in solution, a phenomenon seen mostly for large flexible proteins[17]. Proteins with localised

electrostatic charges may also reorient in order to achieve a packing structure in which favourable interactions are maximised[18]. A key factor in determining the nature of protein adsorption is the degree of hydrophilicity/hydrophobicity of the substrate. In general, a higher protein coverage is seen for hydrophobic surfaces, due to the higher entropy gain of dehydration[19]. However, when electrostatic effects and conformational changes are dominant, significant adsorption may also be observed for hydrophilic surfaces[20,21].

The protein fibrinogen is a key protein in the coagulation process of blood, i.e. in forming the clots that are essential to the body's normal healing process (depicted schematically in Figure 1), and is known to demonstrate significant adhesion to many materials[22]. The dry fibrinogen molecule has a length of 475 Å, and can be thought of as three domains joined by long 'cylinders' (in fact comprising three protein chains each) with diameters of 15 Å. The two end domains have diameters of 65 Å and the central 50 Å[23]. Fibrinogen is present in the blood plasma at an average concentration of around 3 mg mL^{-1} (3000 ppm) and the overall molecular weight is around 340 kDa[24]. The protein is actually a dimer comprising two triplets of polypeptide chains, known as the Aα, Bβ and γ chains, joined in the central domain via disulfide bridges. These disulfide bridges are cleaved by the enzyme thrombin, which is released upon injury to the body, to initiate the polymerisation process that forms a clot[25]. However, upon exposure to a 'foreign body', such as the surface of a biomaterial, the adsorption and change in structure of components such as fibrinogen may result in uncontrolled clot formation, potentially leading to thrombosis.

In this work, the adsorption of fibrinogen on a 316L stainless steel surface is studied using neutron reflectometry and quartz crystal microbalance (QCM) and compared to that on a

chromium oxide surface. Neutron reflectometry is an excellent technique to characterize surface layers of organic species such as proteins; unlike X-rays, which detect elements with high electron density most easily, the scattering length density (SLD) for neutrons is essentially independent of an element's position on the periodic table, and, crucially, varies between isotopes; thus, by varying the isotopic composition of the solvent and/or the adsorbing molecule, different components of the system of interest may be emphasized. SLDs of the species used in this study are summarised in Table 1; further details of the neutron reflectometry technique may be found elsewhere[26,27].

Table 1. SLD values[a]

	ρ / x 10^{-6} Å^{-2}		ρ / x 10^{-6} Å^{-2}
Si	2.072	SiO_2	3.484
Fe	8.020	Fe_2O_3	7.176
Cr	3.027	Cr_2O_3	5.106
Mn	-3.054	Ni	9.406
H_2O	-0.561	D_2O	6.335
fibrinogen / 100% H_2O	1.963	fibrinogen / 100% D_2O	3.264
fibrinogen 50:50 H_2O:D_2O	2.614		

[a](The SLD value of fibrinogen varies depending on the solvent contrast, due to its large number of exchangeable protons.)

To the best of our knowledge, this is the first reported experiment using neutron reflectometry to investigate steel surfaces. This doubtless stems from the challenges of preparing a steel surface suitable for the technique; due to iron's high neutron absorption cross-section[28], only a thin film of steel may be used if the neutron flux is not to be completely lost upon passing through the substrate by the time it reaches the interface and subsequently the detector. Film thicknesses used previously[29–31] for iron films have generally been in the range of 100-300 Å deposited on a supporting silicon block (as silicon does not significantly absorb neutrons). However, whilst this is a relatively straightforward

process for pure metal samples, the deposition of stainless steel films is non-trivial, as it is important to ensure that neither the austenitic phase structure nor the elemental composition are lost during the process; most important is that the surface structure may still be thought of as comparable to that of a real 316L stainless steel sample. The preparation of such films is not entirely novel; Koinkar *et al.* demonstrate the successful deposition of 304 stainless steel (also austenitic) using a laser-beam deposition method, onto a variety of substrates, using X-ray diffraction (XRD) to verify the phase is retained and energy-dispersive X-ray analysis (EDAX) to verify the elemental composition is essentially the same as the original steel sample[32]. Here, in a similar fashion, grazing incidence angle XRD (GIXRD), X-ray photoelectron spectroscopy (XPS), X-ray reflectivity (XRR) and time-of-flight secondary ion mass spectrometry (TOF-SIMS) are used to characterize the deposited stainless steel films and compare to a standard 316L stainless steel sample.

The adsorption of fibrinogen on this stainless steel is further investigated using QCM, which relates changes in frequencies of a resonant crystal upon adsorption of the protein to the mass adsorbed[33].

Experimental

Materials

For all experiments, a physiological model buffer, PBS (phosphate-buffered solution), was used as the solvent and temperatures kept at 37°C throughout to ensure conditions were as would be expected in the body and to prevent protein denaturation. Fibrinogen from bovine plasma was sourced from MP Biomedicals (71 % protein, 7.1 % moisture content) for the QCM measurements and from Sigma (79 % protein, 2.0 % moisture content) for the neutron

reflectometry experiments. In both cases, it was purified by dialysis (using regenerated cellulose tubing - 'SnakeSkin' - with 10K MWCO, acquired from ThermoScientific) for 24 h in phosphate-buffered solution (PBS, 4 x 10 mM NaH_2PO_4, 0.016 M Na_2HPO_4, 0.075 M NaCl) at 0-5°C prior to its immediate use. Protein purities were further verified using gel electrophoresis measurements, which showed no impurities following dialysis.

Stainless steel and chromium films were deposited by electron-beam evaporation at the Nanoscience Centre, University of Cambridge; for the neutron reflectometry experiments, these were deposited onto silicon blocks with dimensions 80 x 50 x 15 mm. For the TOF-SIMS and GIXRD analysis, round silicon blocks were used with 55 mm diameter, 5 mm thickness, and for the XPS measurements the silicon substrates were 10 x 10 x 0.5 mm. 316L stainless steel gaskets were bought from Aalco Metals Ltd., cut into pieces (10 x 10 mm) and used as standards for comparison to the deposited films. 316 stainless steel sensors for the QCM experiments were purchased from Q-sense.

GIXRD

Grazing-incidence X-ray diffraction (GIXRD) experiments were conducted at the Cavendish Laboratories in Cambridge, using a Bruker D8 X-ray diffractometer with copper target and a Goebel mirror. An accelerating voltage of 40 kV was used and a primary beam size of 0.1 mm. 0.35 mm soller slits were inserted before the detector, which was operated in 1D mode. XRR data were fitted using GenX 2.0.0 software[34].

XPS

XPS measurements were taken at the Cavendish Laboratory, Cambridge using a Thermo Scientific ESCALAB 250Xi with a monochromatic Al Kα X-ray source. Samples were cleaned using UV/ozone (30 minutes) prior to measurement. All spectra were calibrated by normalising the C(1s) peak to the standard value of 285.0 eV.

TOF-SIMS

Time of flight secondary ion mass spectroscopy (TOF-SIMS) was carried out using the IONTOF TOF-SIMS V instrument at the Department of Materials, Imperial College London. A dual beam arrangement was used with a voltage of 1 kV at 500 eV. Samples were cleaned using UV/ozone (30 minutes) prior to analysis.

Neutron Reflectometry

Neutron reflectometry data were collected using the D17 instrument at the Institut Laue-Langevin in Grenoble, France[35]. Substrates were cleaned using UV/ozone (30 minutes) prior to immediate cell assembly. The instrument was run in non-polarised, time-of-flight mode with vertically-mounted samples. The beam footprint was 70 x 40 mm (with slits adjusted at each angle to maintain a constant footprint). The substrates were initially characterized under D_2O, H_2O and a 50:50 mixture of the two. Solutions of fibrinogen in PBS/D_2O of increasing concentration, ranging from 5-4000 ppm were then injected into the reflectometry cells (without rinsing between samples to avoid disturbing any adsorbed protein structure). For the 400 and 4000 ppm concentrations, the systems were fully characterized using all three solvent contrasts. At all stages, the protein solutions and neutron cells were kept between 37-39°C. The measurements for each concentration were

started 30 minutes after the protein solution had been introduced into the cell to ensure equilibrium had been attained. Data were fitted using the software RasCAL[36].

QCM

Experiments were performed on a Q-sense E4 QCM at the Nanoscience Centre, University of Cambridge. Custom-made 316 stainless steel sensors were cleaned using 1 % Hellmanex II (30 minutes), rinsed with UPW (ultra-pure water) and dried with N_2, sonicated in 99 % ethanol (10 minutes), rinsed and dried again before final cleaning by UV/ozone (10 minutes). The QCM instrument was cleaned with 2 % Hellmanex and rinsed thoroughly with UPW before the sensors were loaded. The background solution (PBS, 0.01 M) was flowed through all pipework and the sensors were left overnight to equilibrate. After 24 hours, fresh PBS was flowed through and the frequency measured until shown to be stabilised. The sample solution was then flowed through (flow rate 0.15 ml min^{-1}) until the frequency and dissipations were relatively stable. The flow was then stopped and the system left for some minutes to ensure no further changes were seen. At this point, the input solution was reverted to PBS and started again; the frequency was recorded until no further changes were observed. Data were analyzed using the Qtools 3.0 software.

Results and Discussion

GIXRD

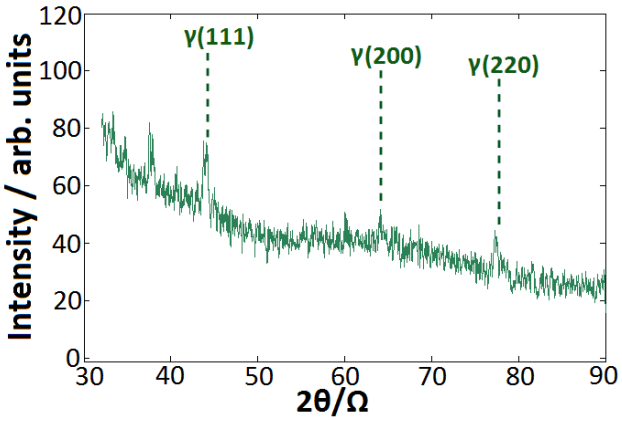

Figure 2. GIXRD spectrum of the deposited steel film at 9°.

GIXRD scans of the deposited stainless steel films were performed over an incidence angle range of 1-9°; the best signal-to-noise ratio was seen at 9°, with the resultant spectrum shown in Figure 2. Resolvable peaks were observed at 2θ = 37.5°, 43.7°, 64.0° and 77.0°, over the 30-90° detector range. This spectrum matches very closely that reported by Silva *et al*. in their powder diffraction pattern for 316L stainless steel[37]. In particular, the peak at 43.7° demonstrates that the phase is indeed austenitic rather than martensitic, which would give rise to a (110) peak around 44.5°, whereas the austenite (111) peak is typically seen around 43.5°, as in this instance[38,39]. The peak at 77.0° is also characteristic of the austenitic phase and may be assigned as the γ-(220) peak[40–43].

XPS

Survey spectra, along with detailed spectra of elements of interest were collected for the deposited surface and compared to those collected for a piece of standard 316L stainless steel. The standard steel sample was hampered by a low signal-to-noise ratio occasioned by its roughness and high levels of adventitious carbon, but a fair comparison of the iron and chromium peaks can be made, as shown in Figure 3, with fit parameters summarised in

Table 2. Whilst no attempt is made here to give a quantitative comparison of the elemental composition (as the relative intensities of the peaks within the survey spectra cannot be taken as a direct measure of relative elemental concentrations[44]), it is useful to compare the types of surface species present in each sample.

Generally for Cr(2p) spectra, only the $2p_{3/2}$ peak is used for quantitative analysis, as there exist satellites and shake-up features that occur at a very similar value for the $2p_{1/2}$ binding energy (around 587 eV) and so are captured within this peak[45]. The Cr(2p) spectra for the deposited film and standard sample are compared in Figure 3a, which clearly shows that a Cr(III) oxide (Cr_2O_3) dominates for both, as reported by the vast majority of the literature[46,47]. The $2p_{3/2}$ peak for unoxidised chromium metal would be expected to occur around 574 eV[6]. From the XPS results here, it is difficult to ascertain whether or not some level of hydroxide is also present, as the reported values for Cr(III) in Cr_2O_3 and $Cr(OH)_3$ in the literature are very similar; binding energies around 576.8 eV are quoted for the $2p_{3/2}$ peak of both[48–50], with 586.2 eV and 587.3 eV for the $2p_{1/2}$ of the oxide and hydroxide respectively[50]. It would seem probable that both species are present here given the values obtained.

As the fitting of Fe(2p) XPS spectra is non-trivial, the key conclusion to be drawn here is the similarity of the two spectra shown in Figure 3b, which highlights the similarity of the deposited layer to the bulk sample as desired, with no attempt at an in-depth analysis of the exact oxidation states present. Some proportion of Fe metal is clearly seen, with a $2p_{3/2}$ peak around 706.5 eV[51], which is presumed to originate from the bulk material underlying the passive oxide layer. The $2p_{3/2}$ peak seen at 711.0-711.2 eV is attributed to the Fe(III)

state, whether in the oxides α-Fe_2O_3 or γ-Fe_2O_3 or a hydroxide, α-FeOOH or γ-FeOOH, all of which have peaks in this region[52–54]. The absence of an additional resolvable peak around 709 eV seems to discount any significant concentrations of magnetite, Fe_3O_4, which comprises a mixture of Fe(II) and Fe(III) ions. In general, the hydroxide peaks are seen at marginally higher binding energies (around 711.5 eV) than those seen here[55,56], and so it is concluded that the dominant species is an iron(III) oxide, with some possible contributions from a surface hydroxide species.

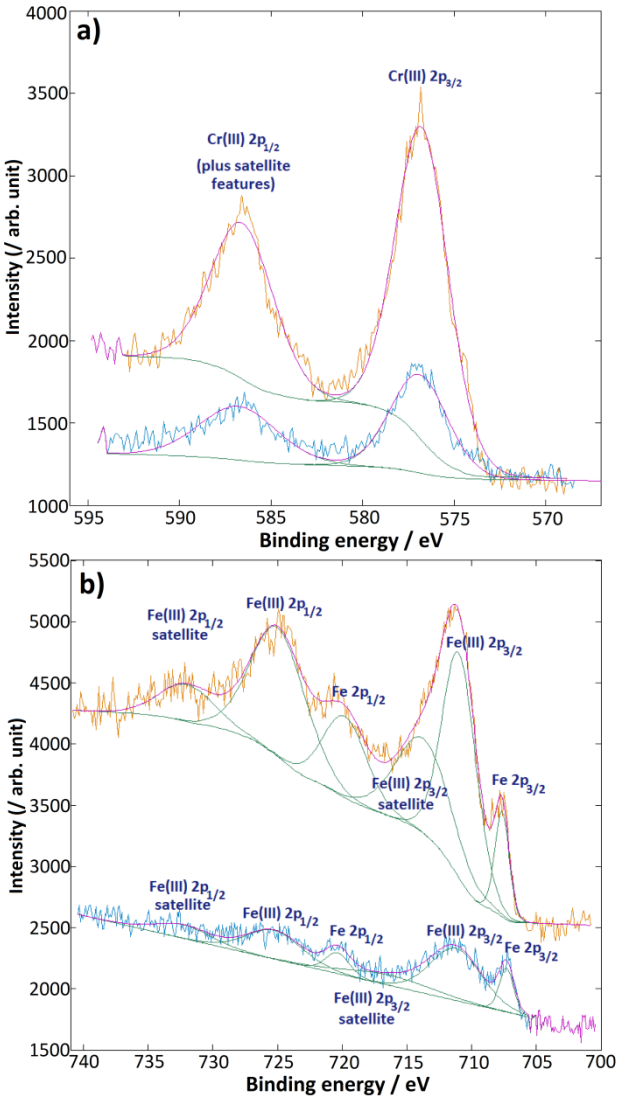

Figure 3. Representative high-resolution XPS spectra for the deposited 316L stainless steel film (orange) and standard steel sample (blue) with individual peak fits shown in green and overall fits in pink for the regions: a) Cr(2p) b) Fe(2p). All spectra are calibrated to the corrected C(1s) peak.

Table 2. Fitted XPS parameters for the deposited steel film and standard steel sample.[a]

Element	Peak	Binding Energy / eV	Area / %	FWHM	Peak Assignment
Deposited film results					
Cr	2p	576.7	62.8	3.5	Cr(III) $2p_{3/2}$
Cr	2p	586.5	37.2	4.3	Cr(III) $2p_{1/2}$
Fe	2p	706.7	5.1	1.3	Fe (metal) $2p_{3/2}$
Fe	2p	711.0	25.7	3.1	Fe(III) $2p_{3/2}$
Fe	2p	713.7	19.3	5.0	Fe(III) $2p_{3/2}$
Fe	2p	719.8	14.5	4.3	satellite
Fe	2p	725.1	26.0	5.0	Fe (metal) $2p_{1/2}$
Fe	2p	732.2	9.4	5.0	Fe(III) $2p_{1/2}$
					Fe(III) $2p_{1/2}$ satellite
Standard steel sample results					
Cr	2p	576.9	57.3	3.6	Cr(III) $2p_{3/2}$
Cr	2p	586.8	42.7	5.0	Cr(III) $2p_{1/2}$
Fe	2p	707.3	9.3	1.3	Fe (metal) $2p_{3/2}$
Fe	2p	711.2	38.8	4.6	Fe(III) $2p_{3/2}$
Fe	2p	715.6	8.9	5.0	Fe(III) $2p_{3/2}$
Fe	2p	720.3	9.9	2.7	satellite
Fe	2p	725.3	22.8	5.0	Fe (metal) $2p_{1/2}$
Fe	2p	732.2	10.4	5.0	Fe(III) $2p_{1/2}$
					Fe(III) $2p_{1/2}$ satellite

[a]'FWHM' represents 'full width at half maximum', i.e. a measure of the peak width

TOF-SIMS

Figure 4 presents a comparison of the TOF-SIMS data for the deposited steel film and the standard steel sample. The TOF-SIMS technique cannot be taken as a quantitative measure of the elemental ratios as each element has a different sensitivity to the sputtering technique. This is normally accounted for by use of relative sensitivity factors (RSFs) - however, as these are only quoted for minute amounts of each element within a matrix (such as silicon or germanium), these are not appropriate in this instance[57]. Instead, the data are presented simply to show how each element varies with depth within the samples.

It is evident that there is a much greater extent of variation, or layering, within the deposited film (Figure 4a) compared to the standard bulk sample, up until the underlying silicon substrate is reached (around 800 s). There are also slight compositional differences; for example, the deposited film has a higher concentration of Mn and lower concentration of Mo than expected (although it should be noted that Mo is about half as sensitive to the TOF-SIMS technique than Mn and Fe, according to their RSF values[57]). This is presumed to arise from their relatively low and high melting points respectively, suggesting that Mo is less susceptible to the electron beam deposition technique, whereas Mn is particularly volatile in comparison to the other steel components. This supposition is supported by the work of Fischmeister *et al*., who note that molybdenum has a lower sputter rate for XPS than other stainless steel elements, possibly for a similar reason[7]. The notable peak in Mn concentration, occurring around a third of the way into the film, is harder to explain, but as this work is concerned with the surface itself, this is not considered a serious issue. Both the deposited film and the standard steel sample (Figure 4b) show a clear decrease in nickel concentration at the surface, as predicted by the literature[10]. In both samples, the iron and chromium signals show very similar trends, with a very slight increase at the surface, again as would be expected. The exact nature of the surface cannot be confidently inferred from the TOF-SIMS data, as an 'equilibration depth', wherein there is a high uncertainty for the measured intensities, is known to exist, thought to be of the order 10 Å into the sample, due to an initial increase in oxygen exposure[57,58]; it is, therefore, necessary to exercise caution in drawing conclusions about the immediate surface from TOF-SIMS data, and hence the XPS data are used rather for this purpose, as described above. Whilst the deposited film clearly differs from a normal piece of steel in terms of the layering within, crucially the surfaces are

found to be comparable; indeed, this complex layered structure in the film ascertained from the SIMS data greatly aids in the neutron reflectometry fitting process, as described below.

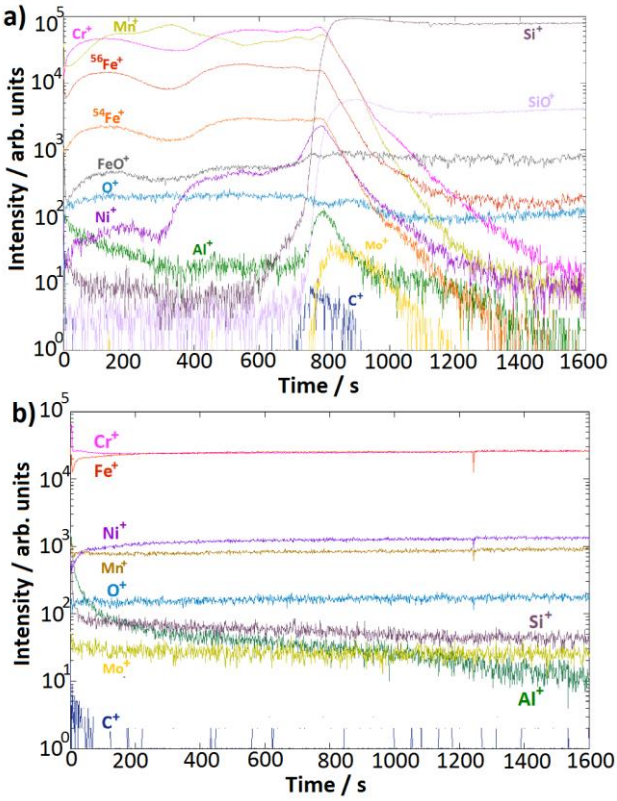

Figure 4. Comparison of TOF-SIMS data for a) the deposited steel film b) the standard 316L steel sample, with elements as labeled. Sputtering time is proportional to the depth through each sample.

Neutron Reflectometry

Steel/water interface

The deposited steel film was initially characterized under three water contrasts: D_2O, H_2O and a 50:50 mixture of the two. The fitted data are shown in Figure 5a with the resultant SLD profile in Figure 5b and fitted parameters summarised in Table 3. The steel film was best described using a fit of 5 layers, with an overall thickness of the film in excellent agreement with that expected by the deposition process and that predicted by XRR data. All SLD values for the fitted layers are lower than what would be expected for pure iron (7.96 x

10^{-6} Å^{-2}) but are reasonable when taking the other elements present into consideration. (For example, chromium has an SLD of 3.031 x 10^{-6} Å^{-2}.) Layer 'c' has a significantly lower SLD than any of the other layers, and is believed to correspond to the manganese-enriched layer observed in the TOF-SIMS data. As manganese has an SLD of -3.001 x 10^{-6} Å^{-2}, only a slight enrichment is necessary to reduce the SLD considerably, as observed. However, the SLD rises again at the surface layer, 'e', indicating, as predicted by the XPS, GIXRD and TOF-SIMS data above, that the surface may be a more reasonable model for an austenitic steel surface. The fitted SLD of around 6.5 x 10^{-6} Å^{-2} is slightly higher than that for a pure chromium oxide Cr_2O_3 layer (5.106 x 10^{-6} Å^{-2}), implying some iron is also present, as would be expected.

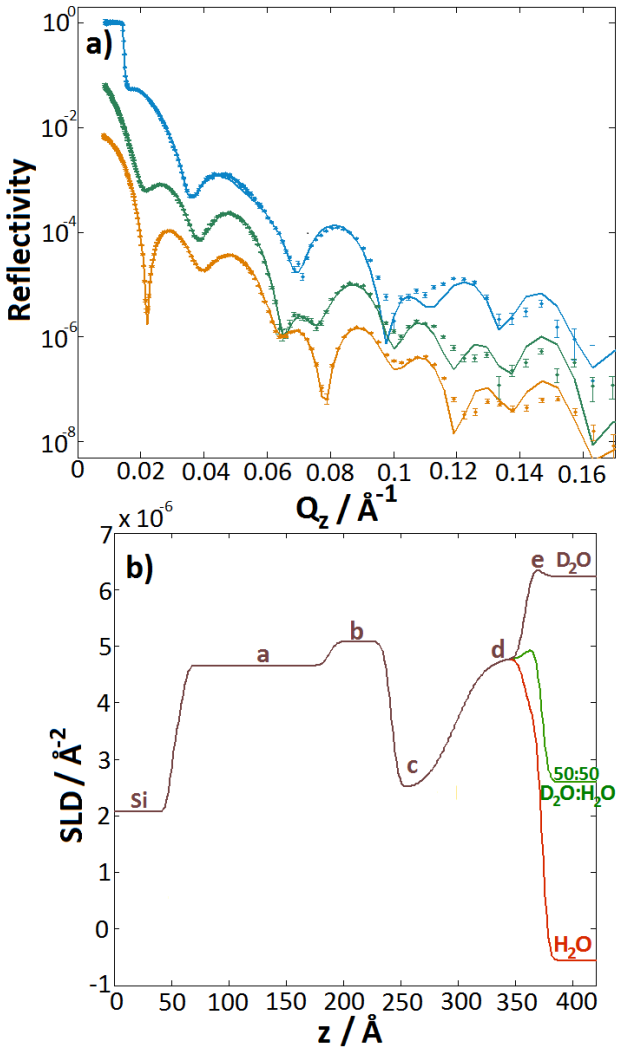

Figure 5.a) Reflectivity profiles for the steel substrate under D_2O, the 50:50 D_2O:H_2O mixture and H_2O in descending order (profiles offset vertically by a factor of 10 for clarity). Data are shown as points with model fits as solid lines. b) SLD profiles for the model fits. The steel film is divided into 5 separate layers, labeled a-e.

Table 3. Fitted parameters for the steel substrate characterized under water, with labels as shown in Figure 5.[a]

	SLD / x 10^{-6} Å^{-2}	Thickness / Å	Roughness / Å	% hydration
SiO_2	3.480	10.0 (± 2)	3.7 (± 2)	0
a	4.653	127.5 (± 2)	4.7 (± 2)	0
b	5.074	54.1 (± 2)	5.0 (± 2)	0
c	2.462	55.9 (± 2)	17.0 (± 2)	0
d	4.783	60.6 (± 2)	4.8 (± 2)	0
e	6.476	15.0 (± 2)	4.2 (± 2)	39 (± 3)

[a]Errors are given as the range of acceptable fits to the data[59].

Adsorption of fibrinogen to 316L stainless steel

Fibrinogen in PBS was subsequently added in increasing concentrations (kept at 37°C throughout) with all concentrations characterized in D_2O, as this was expected to be most sensitive to changes in the protein later. All three contrasts were recorded for concentrations of 400 and 4000 ppm.

Even from concentrations as low as 5 ppm, less than 1 % the physiological concentration, changes were seen in the reflectivity profiles, indicating protein adsorption. For fitting the protein adsorption data, the fitted steel layer parameters were kept constant as described in Table 3. It was found that the best fit to the 400 ppm data, shown in Figure 6, required three layers, all with a high (>75 %) hydration value, as summarised in

Table 4. The middle layer ('F2'), whose centre point lies just over 40 Å from the steel surface, was fitted with the highest concentration of the fibrinogen, sandwiched by two more hydrated layers. When the same approach was extended to the 4000 ppm data, it was necessary to include a fourth layer, with parameters also summarised in

Table 4, suggesting a further diffuse layer adsorbs at high concentrations. Armstrong *et al*. report a similar general model for adsorption of 200 ppm fibrinogen at the silicon/aqueous

interface using neutron reflectometry, with a three-layer model comprising a total thickness of 60 Å and the highest concentration observed for the middle layer[22].

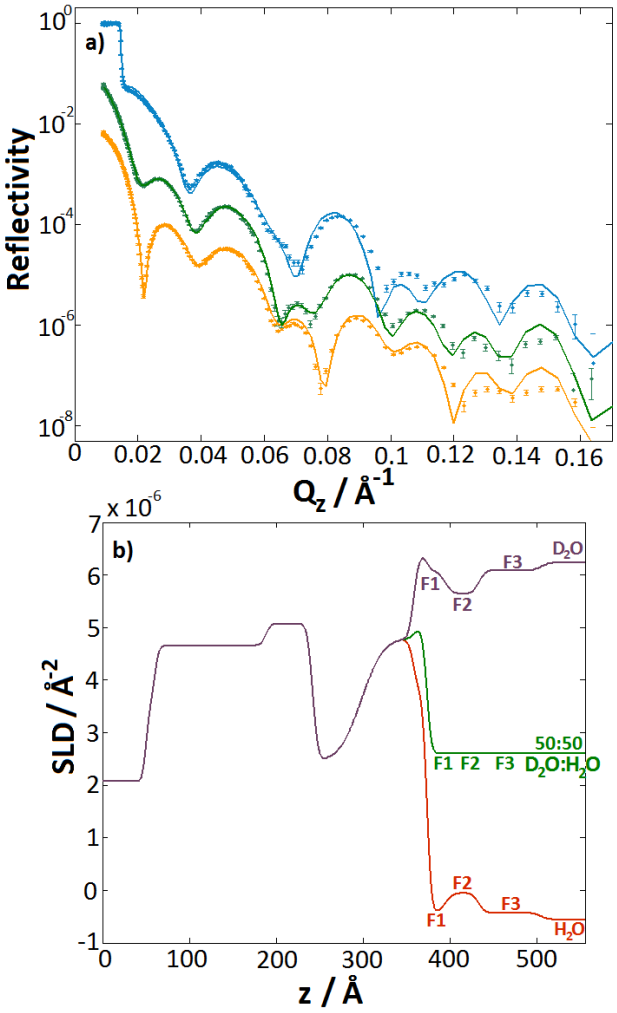

Figure 6. a) Data and model fit for steel with 400 ppm fibrinogen; data shown as points and fits as solid lines. Profiles offset vertically by a factor of 10 for clarity, arranged in the same order as before. b) SLD profiles for the model fits. Fibrinogen layers are labeled as F1 etc., as detailed in

Table 4.

Table 4. Fitted parameters for steel with 400 ppm and 4000 ppm fibrinogen.[a]

Concentration / ppm		Thickness / Å	Roughness / Å	% hydration
400	F1	21.0 (± 2)	7.0 (± 2)	95 (± 3)
	F2	38.7 (± 2)	6.0 (± 2)	80 (± 3)
	F3	72.0 (± 2)	7.0 (± 2)	95 (± 3)
4000	F1	21.0 (± 2)	4.5 (± 2)	92 (± 3)
	F2	37.4 (± 2)	6.0 (± 2)	78 (± 3)
	F3	124.0 (± 2)	2.0 (± 2)	89 (± 3)

F4	100.0 (± 2)	8.0 (± 2)	95 (± 3)

[a]The fitted fibrinogen layers are denoted F1, F2, &c. as shown in Figure 6.

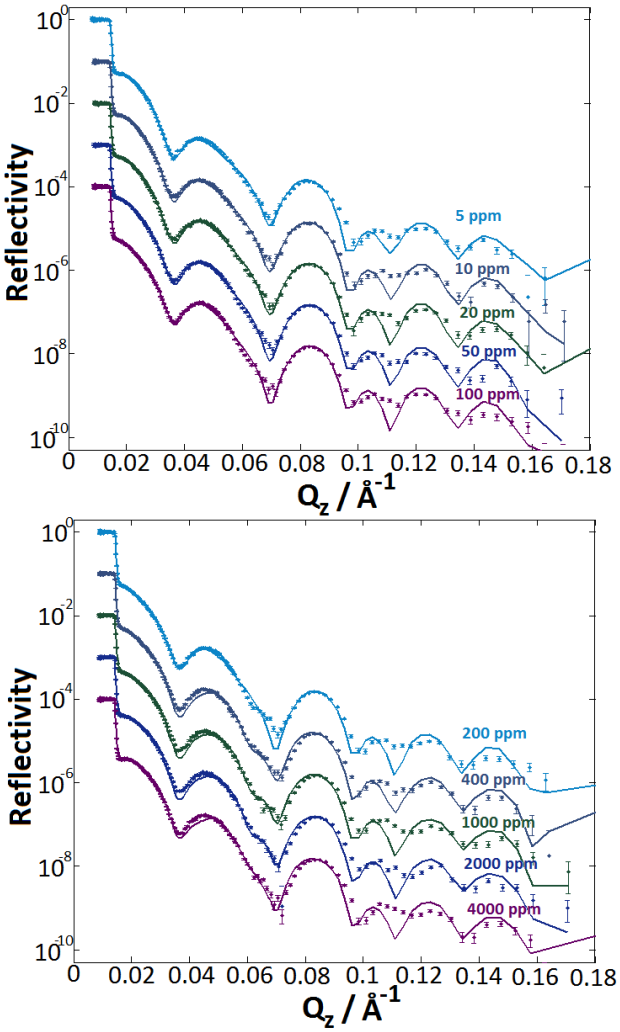

Figure 7. Reflectivity data (points) and fits (solid lines) for all concentrations of fibrinogen on the steel substrate, D_2O contrast only, concentrations as labeled.

All concentrations of fibrinogen (from 5 to 4000 ppm) in D_2O were fitted using this model, with fits shown in Figure 7; the fourth layer was necessary to best describe concentrations higher than 400 ppm. An adsorption isotherm was subsequently generated by calculating the fraction of fibrinogen present in each layer from the hydration value, and assuming the density of fibrinogen to be 1.38 g cm^{-3}. The resultant isotherm showed initial Langmuir-like behavior at low concentrations, but with adsorption increasing as the extra layer was added to the model for samples with concentrations greater than 400 ppm. It was found that the

best isotherm model to describe this layer was the two-step isotherm proposed by Zhu *et al.*[60], whereby the Langmuir and S-shaped isotherm models are combined to give the equation:

$$\nu = \frac{\nu_{max}\, K_1 c(\frac{1}{n} + K_2 c^{n-1})}{1 + K_1 c(1 + K_2 c^{n-1})}$$

where v is the fraction adsorbed, ν_{max} is the maximum fraction adsorbed for the second step, K_1 and K_2 are affinity parameters for the first and second steps respectively, c is the adsorbate concentration and n is a constant analogous to that used in the S-shaped isotherm model; this may relate, for example, to interactions between the adsorbate and solvent, or intra- or inter-molecular interactions for the adsorbate itself[61,62]. The two-step model was developed to describe systems where a further layer of adsorbate not seen at lower concentrations is formed on the surface at higher concentrations, and is hence apposite in this case.

A linear regression was performed on the data for the lower concentrations to extract K_1, ν_{max} was extracted from a linear regression of the higher concentrations and a least squares method was used to determine the remaining parameters K_2 and n. The isotherm data and two-step model fit are shown in Figure 8a. As suggested by the model fit, this would indicate initial formation of a layer close to the surface, with a secondary, highly diffuse later being formed above it at higher concentrations.

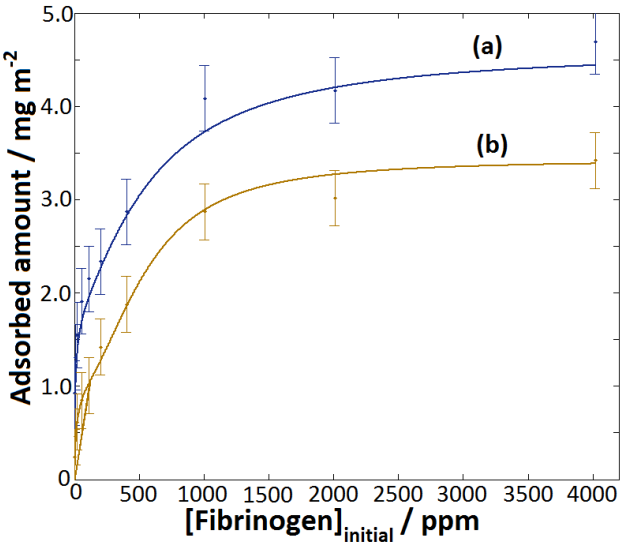

Figure 8. Comparison of the fibrinogen isotherms generated from the neutron reflectometry data on a) 316L stainless steel and b) chromium. Data shown as points, with the two-step isotherm model fits shown as solid lines.

Wertz *et al*. report comparable adsorption coverages for physiological concentrations of fibrinogen (3000 ppm) adsorbed on hydrophilic surfaces[19]. Similarly to this work, they found that irrespective of the surface there was formation of both an irreversibly-bound inner layer and a more diffuse outer layer that was removed upon rinsing. The isotherm coverage values reported here are also in excellent agreement by those reported by Bai *et al*., who used an ex-situ spectroscopic method for determining coverage of fibrinogen on a 316L stainless steel surface[63]. Their estimated layer thicknesses for the protein layers (using ellipsometry) are, however, considerably smaller than those determined by the neutron reflectometry results in this work, being of the order 50 Å, which may correspond to the innermost two protein layers modelled here ('F1' and 'F2'). Intriguingly, they also report a much higher adsorption on titanium surfaces, even though these are usually considered to be more biocompatible than stainless steel. Adamcyzk *et al.* model the adsorption of fibrinogen on an unspecified surface as comprising two distinct steps; firstly the formation of an irreversibly-bound side-on monolayer, followed by a more loosely-bound end-on

monolayer with higher coverage[64]. Although their calculated theoretical maximum adsorption coverages for fibrinogen are of the same order of magnitude as those seen here, their model appears to lack the complexities necessary to completely describe the structure of the adsorbed layer as predicted by the neutron reflectometry results.

Absorption of fibrinogen to chromium oxide

As the surface of 316L stainless steel is believed to be enriched in chromium[4–9], the adsorption of fibrinogen on a deposited chromium film was also studied for comparison. The neutron reflectometry profiles for chromium in D_2O, H_2O and 50:50 D_2O:H_2O mixture show a much simpler profile than that for the steel surface described above, and could be fitted with a chromium layer that was 236 Å thick and a surface chromium oxide (Cr_2O_3) layer that was 23 Å thick, with a 40 Å interlayer; the fits and SLD profiles are shown in Figure 9, with fit parameters summarised in Table 5. The thickness of the passive oxide film is thought to depend on the metal in question, with typical figures of 4, 2 and 1 nm quoted for iron, stainless steel alloys and chromium respectively[65]. The thickness fitted here for the Cr_2O_3 layer is rather higher than this, presumed to be a consequence of the UV/ozone cleaning process. The fitted SLD values are very close to those theoretically expected for Cr and Cr_2O_3 (Table 1).

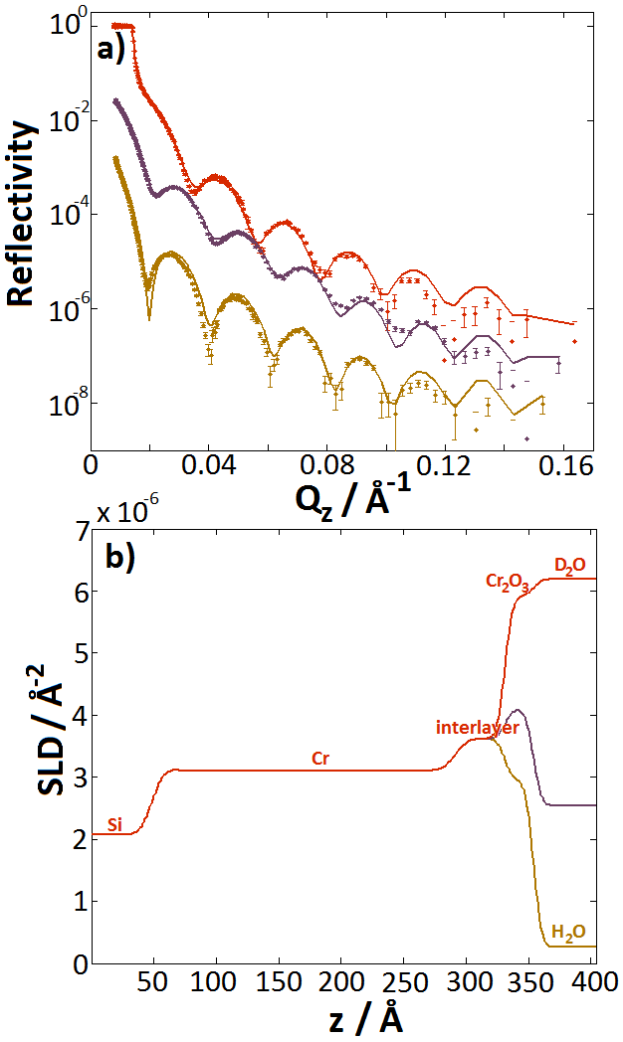

Figure 9. a) Reflectivity profiles for the deposited chromium layer under D_2O, the 50:50 D_2O:H_2O mixture and H_2O in descending order (profiles offset vertically for clarity). Data are shown as points with models as solid lines. b) SLD models for the model fits.

Table 5. Fitted parameters for the deposited chromium film characterized under water, with labels as shown in Figure 9.

	SLD / x 10^{-6} Å^{-2}	Thickness / Å	Roughness / Å	% hydration
Cr	3.15	236.2 (± 2)	8.0 (± 2)	0
interlayer	3.62	40.0 (± 2)	8.0 (± 2)	0
Cr_2O_3	5.64	23.0 (± 2)	5.0 (± 2)	48 (± 3)

When the fibrinogen solutions were added to the chromium substrate, clear changes were again seen in the reflectivity profiles for the D_2O contrasts, indicating protein adsorption. Similarly to the adsorption structure described above, for concentrations up to 400 ppm the best fit to the data was achieved using a three-layer block model; from 400 to 4000 ppm, a further diffuse layer was necessary. The fitted reflectivity and SLD profiles for the 400 ppm

concentration under both water contrasts are shown in Figure 10 with fit parameters for 400 and 4000 ppm concentrations summarised in

Table 6.

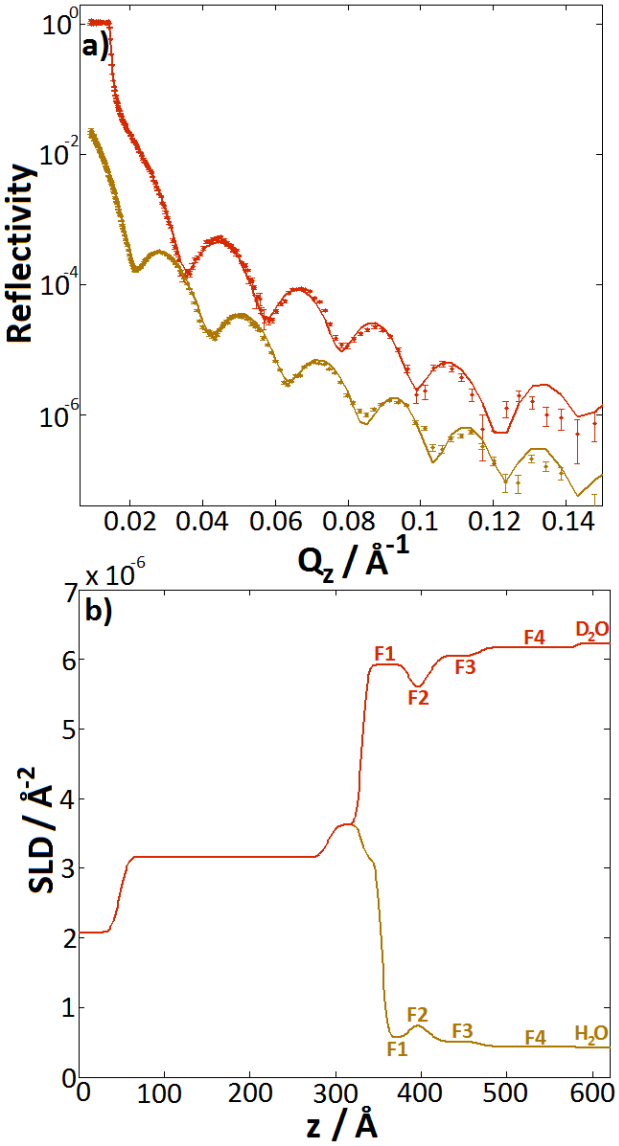

Figure 10. a) Fitted reflectivity profiles showing the four fibrinogen layers for 400 ppm fibrinogen on chromium. b) Corresponding SLD profiles.

Table 6. Fitted parameters for chromium with 400 and 4000 ppm fibrinogen, where the fibrinogen layers are labeled as F1, F2 &c., as shown in Figure 10

Concentration / ppm		Thickness / Å	Roughness / Å	% hydration
400	F1	32.4 (± 2)	6.2 (± 2)	90 (± 3)
	F2	23.0 (± 2)	7.4 (± 2)	77 (± 3)
	F3	60.0 (± 2)	7.7 (± 2)	94 (± 3)
	F4	112.0 (± 2)	3.0 (± 2)	98 (± 3)
4000	F1	26.2 (± 2)	6.5 (± 2)	86 (± 3)
	F2	36.0 (± 2)	9.2 (± 2)	78 (± 3)
	F3	64.3 (± 2)	8.5 (± 2)	90 (± 3)
	F4	116.6 (± 2)	10.0 (± 2)	94 (± 3)

.

As for the steel substrate, a range of fibrinogen concentrations (5-4000 ppm) were characterized in D_2O. Again, it was found that the two-step isotherm gave a good fit to the calculated isotherm data, shown in Figure 8b. It is interesting to note that the coverage of fibrinogen on chromium is significantly lower than that seen for the steel surfaces. There is significantly less literature concerning the adsorption of proteins onto chromium than onto steel, although Cuypers *et al.* report some ellipsometric results for fibrinogen layers on pure chromium and chromium oxides, with equilibrium protein thicknesses of around 30 and 130 Å respectively at a concentration of 10 ppm fibrinogen[66]. The overall fitted thickness for the 10 ppm fibrinogen on the chromium film in this work lies in between these values, at 56 Å.

Despite the lower overall coverage of fibrinogen on the chromium surface than on the steel surface, the general adsorption behavior is comparable, with a sandwich-like structure encompassing the layer of highest concentration, and thicker, more diffuse layers seen at higher concentrations. This seems to indicate the fibrinogen is adopting a similar adsorbed layer structure as on the steel, which may lend weight to the theories stating that the most important factor in determining protein adsorption is the hydrophobicity/hydrophilicity of the surface[21,67]. As the contact angles for the oxides at the surfaces of both films are not

likely to differ substantially, the same components of the protein are likely to preferentially adhere thereupon in both cases.

QCM

Two concentrations of fibrinogen in PBS (400 and 4000 ppm) were measured using QCM on a 316 stainless steel surface. The frequency plots against time are shown superimposed in Figure 11; the times at which the flow of the fibrinogen solutions and PBS solutions were started are marked with arrows, and the different overtones (F1, F3 &c.) are marked on the plots. For 4000 ppm, a large frequency change was observed upon introduction of the fibrinogen, revealing significant adsorption had occurred. The frequency stabilised fairly promptly, indicating that equilibration was reached rapidly; this accords with the general understanding that protein adsorption to foreign body surfaces occurs within seconds, and with the neutron reflectometry data (as profiles recorded after 30 minutes equilibration time were identical to those recorded 3 hours later). When the fibrinogen solution was exchanged for PBS solution again, a significant proportion of the layer was removed, demonstrated by the frequency returning closer to its initial value. Similarly, upon introduction of the 400 ppm sample, a sizeable change in frequency was seen, evincing adsorption to the steel surface. When PBS was reflowed through the system, the frequency was again seen to revert slightly towards its starting value, implying some of the adsorbed protein was removed. However, the extent of removal was clearly less than for the 4000 ppm sample.

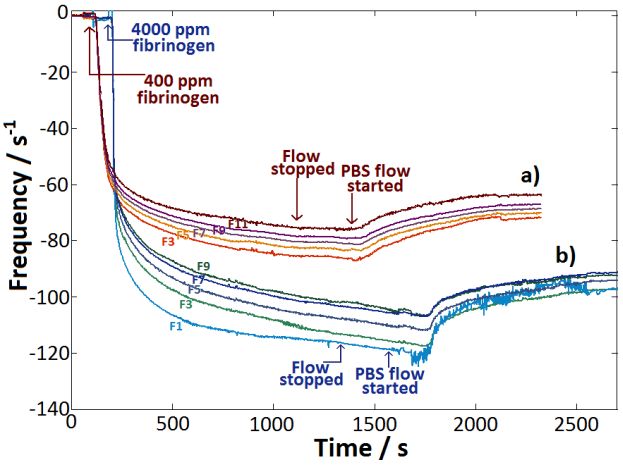

Figure 11. QCM frequency plots for a) 400 ppm and b) 4000 ppm fibrinogen, superimposed to show relative changes. F1, F3 &c. refer to the frequency overtones.

Both Sauerbrey[68] and Voigt viscoelastic[33] equations were used to model the datasets, with the resultant mass change plots as a function of time shown in Figure 12. However, as relatively large changes in dissipation were measured for both protein concentrations, and the dissipations for each overtone did not overlap in either case, it is unlikely that the adsorbed protein formed the rigid layers assumed by the Sauerbrey equation, and hence the Voigt model was believed to be more appropriate, as shown by the good fits to the data in Figure 13 (whereby the protein density was kept constant at 1.38 g mL^{-1} and the viscosity, shear and mass fitted). As expected, the masses calculated using the Voigt model are significantly larger than for the Sauerbrey, indicating a more disperse adsorption structure rather than a rigid film, in keeping with the highly diffuse layers predicted by the neutron reflectometry fits.

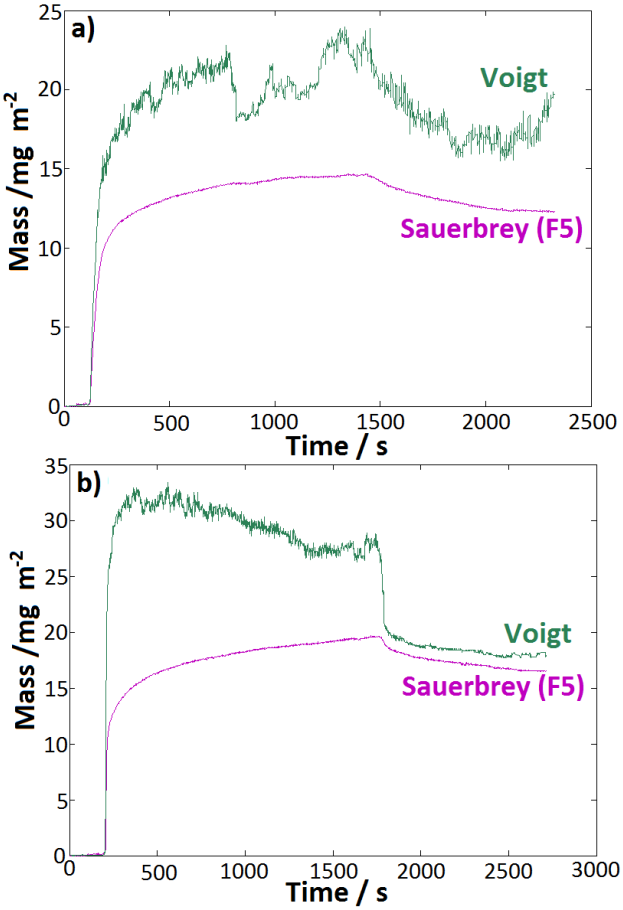

Figure 12. Voigt (green) and Sauerbrey (pink, modelled using the F5 overtone) fitted layer masses for a) 400 ppm and b) 4000 ppm fibrinogen. (Note the difference in y-axis between the plots.)

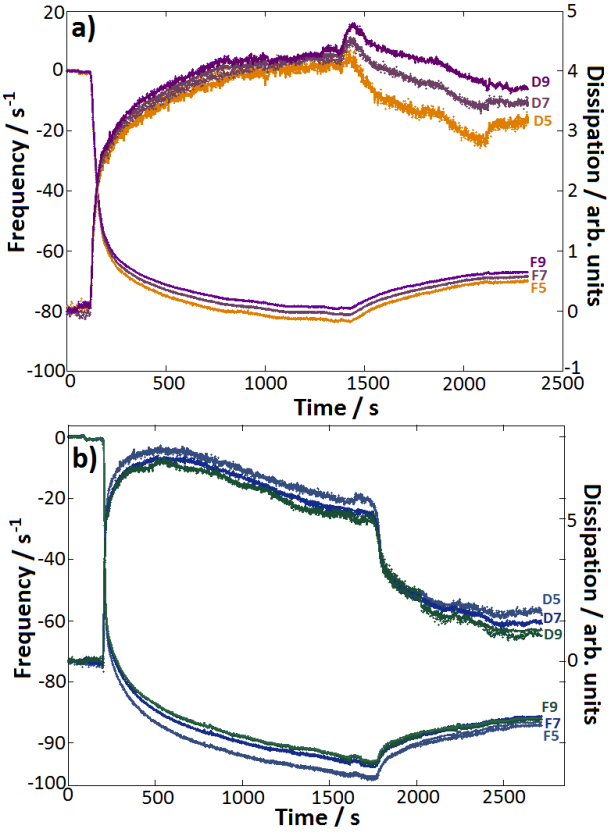

Figure 13. Frequency and dissipation data (+) and Voigt model fits (solid lines) for a) 400 ppm and b) 4000 ppm fibrinogen, overtones as labeled.

The masses predicted by the QCM modelling are much higher than those derived from the neutron reflectometry data, irrespective of the model used. This is a phenomenon commonly reported in the literature, and observed particularly for protein adsorption, due to their ability to trap large volumes of solvent, which are included in the mass sensed by the QCM, whereas the neutron reflectometry technique is able to distinguish between the protein and any trapped water. Even such large discrepancies as the order of magnitude increase seen here are not unusual, particularly for proteins that have unfolded upon adsorption[69]. The mass values calculated according to the QCM data presented here should, therefore, be taken as hydrated values, whereas the mass values according to the neutron data may be presumed as absolute mass of the unhydrated protein. The particularly high values for the hydrated masses seen here may, therefore, be an indication of protein

deformation and unfolding on the surface, as this would increase the extent of its water retention. Desroches *et al*. report IR studies of adsorbed fibrinogen on 316L stainless steel wherein they observe a decrease in the signals pertaining to α-helix and β-sheet content, accompanied by an increase in β-turn concentration, signifying extensive conformational change. This was seen to occur in the first 10 minutes of adsorption and reached equilibrium shortly afterwards, also in good agreement with the observations detailed herein[67].

The QCM data, whilst not providing reliable quantification of adsorbed protein masses, is helpful in confirming the adsorption mechanism inferred from the neutron reflectometry data. Relatively speaking, there is clearly a significantly greater amount of protein adsorption at 4000 ppm than at 400 ppm, in good agreement with the two-step isotherm model derived from the neutron reflectometry data. This is further supported by the extent of protein removal upon 'washing' with the PBS solution. The higher proportion of protein that is removed by washing for the 4000 ppm sample supports the proposal of a further diffuse layer seen at higher concentrations that is not so strongly adhered to the surface. The tendency of the Voigt-modelled mass to return to values close to those predicted by the Sauerbrey upon washing in the case of the higher concentration (Figure 12b) implies that after washing, the film may be described more accurately as a rigid-type film and that it is the diffuse outerlayer that has been removed. Even so, the washing is evidently insufficient to remove more than a fraction at either concentration, demonstrating the adsorption of layers closest to the surface is irreversible when no other competing protein is present.

Conclusions

Whilst the TOF-SIMS plots of the deposited 316L stainless steel film showed greater elemental variation below the surface when compared to a standard steel sample, the XPS spectra confirmed the surface compositions were essentially the same, and the GIXRD results demonstrated the austenitic phase had been retained, suggesting that the films deposited using the electron beam method provide a viable model for the actual steel surface. To the best of our knowledge, this is the first reported neutron reflectometry study of stainless steel, an indubitably important material across numerous fields.

The neutron reflectometry results for both stainless steel and chromium surfaces required a model fit incorporating three or four protein layers, with the most concentrated sitting a distance of around 20 Å from the surface. Whilst it is possible here to rule out such binding models as a simple end-on or side-on configuration due to the incongruity of the fitted layer parameters from the neutron data compared to the dimensions of the fibrinogen molecule, it remains difficult to draw any definite conclusions as to the exact binding nature of the fibrinogen proteins to the steel surface. The high water retention of the protein demonstrated by both QCM and neutron reflectometry data suggests that the protein may be at least partially unfolded or denatured, a phenomenon often observed for protein adsorption. Wertz *et al.* have reported adsorption on both hydrophobic and hydrophilic surfaces of a broad range of fibrinogen conformations with denaturation and reorientation occurring on each respectively as a function of time[70]. From the overall thicknesses of the protein layers (100-250 Å) modelled here, it would seem likely that the adsorbed layer comprises some form of coiled or unfolded structure/structures (for example, in the simplistic schematic shown in the Table of Contents figure).

The plotted isotherm derived from the neutron reflectometry data for the fibrinogen/steel system gives an adsorbed amount of between 4 and 4.5 mg m^{-2} for the physiological concentration of 3000 ppm, in good agreement with the literature[19,63,64]. A lower adsorption coverage is seen for the chromium oxide surface, proving that, whilst there is a chromium enrichment at the surface of stainless steel, using a chromium film alone cannot be considered a suitable model. The structural model fits were, however, almost identical for both surfaces. The QCM results for the fibrinogen/stainless steel system confirmed the existence of a diffuse, irreversibly-bound layer at higher concentrations, with the inner layer formed at lower concentrations remaining after rinsing.

Acknowledgements

The authors are thankful to the Nanoscience Centre, University of Cambridge for access to the QCM and to Dr Myriam Ouberai for her assistance in using the instrument. We are also grateful to Dr Fanny Yuen for electrophoretic measurements. Neutron reflectometry data were acquired on the D17 instrument at the Institut Laue-Langevin (experiment number 9-13-550; doi:10.5291/ILL-DATA.9-13-550). MHW is grateful to the Oppenheimer Trust for funding.

Supporting Information Available Neutron reflectometry data for 100 ppm fibrinogen/steel demonstrating lack of change after 3 hours as compared to after 30 minutes. This material is available free of charge via the Internet at http://pubs.acs.org.

Bibliography

(1) Lane, W. A. Some remarks on the treatment of fractures. *Brit. Med. J.* **1895**, *1*, 861-863.

(2) Disegi, J. A.; Eschbach, L. Stainless steel in bone surgery. *Injury* **2000**, *31*, S–D2-D6.

(3) Kurella, A.; Dahotre, N. B. Review paper: surface modification for biomplants: the role of laser surfae engineering. *J. Biomater. Appl.* **2005**, *20*, 5-50.

(4) Fredriksson, W. Depth profiling of the passive layer on stainless steel using photoelectron spectroscopy, Ph.D. Thesis, Uppsala Universitet, 2012.

(5) Park, R. L.; Houston, J. E.; Schreiner, D. G. Chromium depletion of vacuum annealed stainless steel surfaces *J. Vac. Sci. Technol.* **1972**, *9*, 1023-1027.

(6) Rossi, A.; Elsener, B.; Hähner, G.; Textor, M.; Spencer, N. D. XPS, AES and ToF-SIMS investigation of surface films and the role of inclusions on pitting corrosion in austenitic stainless steels. *Surf. Int. Anal.* **2000**, *29*, 460-467.

(7) Fischmeister, H.; Roll, U. Passivschichten auf rostfreien stählen: eine übersicht über oberflächenanalytische ergebnisse *Fresenius Z. Anal. Chem.* **1984**, *319*, 639-645.

(8) Olsson, C.-O. A.; Landolt, D. Passive films on stainless steels - chemistry, structure and growth. *Electrochim. Acta* **2003**, *48*, 1093-1104.

(9) Duarte, M. J.; Klemm, J.; Klemm, S. O.; Mayrhofer, K. J. J.; Stratmann, M.; Borodin, S.; Romero, A. H.; Madinehei, M.; Crespo, D.; Serrano, J. et al. Element-resolved corrosion analysis of stainless-type glass-forming steels. *Science* **2013**, *341*, 372-376.

(10) Olefjord, I.; Elfstrom, B.-O. The composition of the surface during passivation of stainless steels. *Corrosion* **1982**, *38*, 46-52.

(11) Frankenthal, R. P.; Maim, D. L. Analysis of the air-formed oxide film on a series of iron-chromium alloys by ion-scattering spectrometry. *J. Electrochem. Soc.* **1976**, *123*, 186-191.

(12) Taubert, A.; Mano, J. F.; Rodríguez-Cabello, J. C. *Biomaterials Surface Science*; Wiley-VCH Verlag GmbH & Co. KGaA: Weinheim, 2013.

(13) *Biomaterials Science*; Ratner, B. D., Hoffman, A. S., Schoen, F. J., Lemons, J. E., Eds.; Elsevier Academic Press: Sandiego, London, 2004.

(14) Wilson, C. J.; Clegg, R. E.; Leavesley, D. I.; Pearcy, M. J. Mediation of biomaterial-cell interactions by adsorbed proteins: a review. *Tissue Eng.* **2005**, *11*, 1-18.

(15) Yu, J.-L.; Andersson, R.; Ljungh, A. Protein adsorption and bacterial adhesion to biliary stent materials. *J. Surg. Res.* **1996**, *62*, 69-73.

(16) Anderson, J. A.; Rodriguez, A.; Chang, D. T. Foreign body reaction to biomaterials. *Semin. Immunol.* **2008**, *20*, 86-100.

(17) Ramsden, J. Puzzles and paradoxes in protein adsorption. *Chem. Soc. Rev.* **1995**, *24*, 73-78.

(18) Rabe, M.; Verdes, D.; Seeger, S. Understanding protein adsorption phenomena at solid surfaces. *Adv. Colloid Interface Sci.* **2011**, *162,* 87-106.

(19) Wertz, C. F.; Santore, M. M. Effect of surface hydrophobicity on adsorption and relaxation kinetics of albumin and fibrinogen: single-species and competitive behavior. *Langmuir* **2001**, *17*, 3006-3016.

(20) Buijs, J.; Norde, W.; Lichtenbelt, J. W. T. Changes in the secondary structure of adsorbed IgG and F(ab')$_2$ studied by FTIR spectroscopy. *Langmuir* **1996**, *12*, 1605-1613.

(21) Weidner, T.; Castner, D. G. SFG analysis of surface bound proteins: a route towards structure determination. *Phys. Chem. Chem. Phys.* **2013**, *15*, 12516-12524.

(22) Armstrong, J.; Salacinski, H. J.; Mu, Q.; Seifalian, A. M.; Peel, L.; Freeman, N.; Holt, C. M.; Lu, J. R. Interfacial adsorption of fibrinogen and its inhibition by RGD peptide: a combined physical study. *J. Phys. Condens. Matter* **2004**, *16*, S2483-S2491.

(23) Hall, B. C. E.; Ph, D.; Slayter, H. S. The fibrinogen molecule : its size , shape , and mode of polymerization. *J. Biophys. Biochem. Cytol.* **1959**, *5*, 11-17.

(24) Cieśla, M.; Adamczyk, Z.; Barbasz, J.; Wasilewska, M. Mechanisms of fibrinogen adsorption at solid substrates at lower pH. *Langmuir* **2013**, *29*, 7005-7016.

(25) Dee, K. C.; Puleo, D. A.; Bizios, R. *An Introduction to Tissue-Biomaterial Interactions*; John Wiley & Sons Inc.: New Jersey, 2002.

(26) Penfold, J.; Thomas, R. K. The application of the specular reflection of neutrons to the study of surfaces and interfaces. *J. Phys. Condens. Matter* **1990**, *2*, 1369-1412.

(27) Penfold, J.; Thomas, R. K.; Lu, J. R.; Staples, E.; Tucker, I.; Thompson, L. The study of surfactant adsorption by specular neutron reflection. *Phys. B.* **1994**, *198*, 110-115.

(28) Ross, M.; Story, J. S. Slow neutron absorption cross sections of the elements. *Rep. Prog. Phys.* **1949**, *12*, 291-304.

(29) Wood, M. H.; Welbourn, R. J. L.; Charlton, T.; Zarbakhsh, A.; Casford, M. T.; Clarke, S. M. Hexadecylamine adsorption at the iron oxide-oil interface. *Langmuir* **2013**, *29*, 13735-13742.

(30) Wood, M. H.; Casford, M. T.; Steitz, R.; Zarbakhsh, A.; Welbourn, R. J. L.; Clarke, S. M. Comparative adsorption of saturated and unsaturated fatty acids at the iron oxide/oil interface. *Langmuir* **2016**, *32,*, 534–540.

(31) Wood, M. H.; Welbourn, R. J. L.; Zarbakhsh, A.; Gutfreund, P.; Clarke, S. M. Polarised neutron reflectometry of nickel corrosion inhibitors, *Langmuir* **2015**, *31*, 7062-7072.

(32) Koinkar, V. N.; Chaudhari, S. M.; Kanetkar, S. M.; Ogale, S. B. Deposition of stainless steel film using pulsed laser. *Thin Solid Films* **1989**, *171*, 335-342.

(33) Voinova, M. V; Rodahl, M.; Jonson, M.; Kasemo, B. Viscoelastic acoustic response of layered polymer films at fluid-solid interfaces: continuum mechanics approach. *Phys. Scr.* **1999**, *59*, 391-413.

(34) Björck, M.; Andersson, G. GenX: an extensible X-ray reflectivity refinement program utilising differential evolution. *J. Appl. Cryst.* **2007**, *40*, 1174-1178.

(35) Cubitt, R.; Fragneto, G. D17: the new reflectometer at the ILL. *Appl. Phys. A* **2002**, *74*, S329-S331.

(36) Hughes, A. V. RasCAL, 2013. Sourceforge. Downloaded from: http://

sourceforge.net/projects/rscl/. (accessed March 3, 2016)

(37) Silva, G.; Baldissera, M. R.; Trichês, E. D. S.; Cardoso, K. R. Preparation and characterization of stainless steel 316L/HA biocomposite. *Mat. Res.* **2013**, *16*, 304-309.

(38) Cheary, R. W.; Ma-Sorrell, Y. Quantitative phase analysis by X-ray diffraction of martensite and austenite in strongly oriented orthodontic stainless steel wires *J. Mat. Sci.* **2000**, *35*, 1105-1113.

(39) Leone, G. L.; Kerr, H. W. The ferrite to austenite transformation in stainless steels. *Weld. J. Res. Suppl.* **1981**, 13s-21s.

(40) Solomon, N.; Solomon, I. Deformation induced martensite in AISI 316 stainless steel. *Rev. Met. Madrid* **2010**, *46*, 121-128.

(41) Abreu, H. F. G. de; Carvalho, S. S.; Neto, P. de L.; Santos, P. dos S.; Freire, V. N.; Silva, P. M. de O.; Tavares, S. S. M. Deformation induced martensite in an AISI 301LN stainless steel: characterization and influence on pitting corrosion resistance. *Mat. Res.* **2007**, *10*, 359-366.

(42) Furlan, K. P.; Binder, C.; Klein, A. N.; Daniel, J.; Mello, B. De. Thermal stability of the MoS_2 phase in injection moulded 17-4 PH stainless steel. *J. Mater. Res. Technol.* **2012**, *1*, 134-140.

(43) Sha, C.-H.; Lee, C. C. Microstructure and surface treatment of 304 stainless steel for electronic packaging. *J. Electron. Packag.* **2011**, *133*, 021005–1-4.

(44) Wagner, C. D.; Davis, L. E.; Zeller, M. V.; Taylor, J. A.; Raymond, R. H.; Gale, L. Empirical atomic sensitivity factors for quantitative analysis by electron spectroscopy for chemical analysis. *Surf. Int. Anal.* **1981**, *3*, 211-225.

(45) Salvi, A. M.; Castle, J. E.; Watts, J. F.; Desimoni, E. Peak fitting of the chromium 2p XPS spectrum. *Appl. Surf. Sci.* **1995**, *90*, 333-341.

(46) Adams, R. O. A review of the stainless steel surface. *J. Vac. Sci. Technol.* **1983**, *1*, 12-18.

(47) Barnhart, J. Occurrences, uses and properties of chromium. *Regul. Toxicol. Pharm.* **1997**, *26*, S3-S7.

(48) Elsener, B.; DeFilippo, D.; Rossi, A. In *Modifications of Passive Films*; Marcus, P., Baroux, B., Keddam, M., Eds.; EFC Publ.: London, 1994; pp 6–11.

(49) Pancotti, A.; de Siervo, A.; Carazzolle, M. F.; Landers, R.; Kleiman, G. G. Ordered oxide surfaces on metals: chromium oxide. *Top. Catal.* **2011**, *54*, 90-96.

(50) Gao, X.; Wu, X.; Zhang, Z.; Guan, H.; Han, E. Characterization of oxide films grown on 316L stainless steel exposed to H_2O_2-containing supercritical water. *J. Supercrit. Fluids* **2007**, *42*, 157-163.

(51) Hawn, D. D.; DeKoven, B. M. Deconvolution as a correction for photoelectron inelastic energy losses in core level XPS spectra of iron oxides. *Surf. Int. Anal.* **1987**, *10*, 63-74.

(52) Paparazzo, E. XPS and auger spectroscopy studies on mixtures of the oxides SiO_2, Al_2O_3, Fe_2O_3 and Cr_2O_3. *J. Electron Spectrosc. Rel. Phenom.* **1987**, *43*, 97-112.

(53) Grosvenor, A. P.; Kobe, B. A.; Biesinger, M. C.; McIntyre, N. S. Investigation of multiplet splitting of Fe 2p XPS spectra and bonding in iron compounds. *Surf. Int. Anal.* **2004**, *36*, 1564-1574.

(54) Brion, D. Etude par spectroscopie de photoelectrons de la degradation superficielle de FeS_2, $CuFeS_2$, ZnS et PbS a l'air et dans l'eau. *Appl. Surf. Sci.* **1980**, *5*, 133-152.

(55) Konno, H.; Nagayama, M. X-ray photoelectron spectra of hexavalent iron. *J. Electron Spectrosc. Rel. Phenom.* **1980**, *18*, 341-343.

(56) Tan, B. T.; Klabunde, K. J.; Sherwood, P. M. A. X-ray photoelectron spectroscopy studies of solvated metal atom dispersed catalysts. Monometallic iron and bimetallic iron-cobalt particles on alumina. *Chem. Mat.* **1990**, *2*, 186-191.

(57) Wilson, R. G.; Stevie, F. A.; Magee, C. W. *Secondary Ion Mass Spectrometry: a practical handbook for depth profiling and bulk impurity analysis*; John Wiley & Sons Inc.: USA, 1989.

(58) Wittmaack, K. Aspects of quantitative secondary ion mass spectrometry. *Nucl. Instr. and Meth.* **1980**, *168*, 343–356.

(59) Wadsäter, M.; Barker, R.; Mortensen, K.; Feidenhans'l, R.; Cárdenas, M. Effect of phospholipid composition and phase on nanodisc films at the solid-liquid interface as studied by neutron reflectivity. *Langmuir* **2013**, *29*, 2871–2880.

(60) Zhu, B.; Gu, T. Surfactant adsorption at solid-liquid interfaces. *Adv. Colloid Interface Sci.* **1991**, *37*, 1-32.

(61) Sposito, G. *The Chemistry of Soils*; Oxford University Press: New York, 2008.

(62) Nakagaki, M.; Handa, T.; Shimabayashi, S. S-shaped adsorption isotherms of surface active electrolytes from aqueous solutions. *J. Coll. Int. Sci.* **1973**, *43*, 521-529.

(63) Bai, Z.; Filiaggi, M. J.; Dahn, J. R. Fibrinogen adsorption onto 316L stainless steel, nitinol and titanium. *Surf. Sci.* **2009**, *603*, 839-846.

(64) Adamczyk, Z.; Barbasz, J.; Cieśla, M. Mechanisms of fibrinogen adsorption at solid substrates. *Langmuir* **2011**, *27*, 6868-6878.

(65) Holliday, J. E.; Frankenthal, R. P. Characterization of passivating films on Fe-Cr alloys by soft X-ray spectroscopy. *J. Electrochem. Soc.* **1972**, *119*, 1190-1192.

(66) Cuypers, P. A.; Hermens, W. T.; Hemker, H. C. Ellipsometric study of protein film on chromium. *Ann. New York Acad. Sci.* **1977**, *283*, 77-85.

(67) Desroches, M.-J.; Omanovic, S. Adsorption of fibrinogen on a biomedical-grade stainless steel 316LVM surface: a PM-IRRAS study of the adsorption thermodynamics, kinetics and secondary structure changes. *Phys. Chem. Chem. Phys.* **2008**, *10*, 2502-2512.

(68) Knag, M.; Sjöblom, J.; Øye, G.; Gulbrandsen, E. A quartz crystal microbalance study of the adsorption of quaternary ammonium derivatives on iron and cementite. *Coll. Surf. A* **2004**, *250*, 269-278.

(69) Ouberai, M. M.; Xu, K.; Welland, M. E. Effect of the interplay between protein and surface on the properties of adsorbed protein layers. *Biomat.* **2014**, *35*, 6157-6163.

(70) Wertz, C. F.; Santore, M. M. Fibrinogen adosrption on hydrophilic and hydrophobic surfaces: geometrical and energetic aspects of interfacial relaxations. *Langmuir* **2002**, *18*, 706-715.

Table of contents graphic